McKelvey School of Engineering Theses & Dissertations

McKelvey School of Engineering

Summer 8-2016

Contact Radius and Insulator-Metal Transition in Films Comprised of Touching Semiconductor Nanocrystals

Deanna M. Lanigan
Washington University in St. Louis

WASHINGTON UNIVERSITY IN ST. LOUIS

School of Engineering and Applied Science

Department of Energy, Environmental, and Chemical Engineering

Thesis Examination Committee:
Elijah Thimsen
Pratim Biswas
Bryce Sadtler

Contact Radius and Insulator-Metal Transition in Films

Comprised of Touching Semiconductor Nanocrystals

by

Deanna Lanigan

A thesis presented to the School of Engineering
of Washington University in St. Louis in partial fulfillment of the
requirements for the degree of
Master of Science

August 2016

Saint Louis, Missouri

Contents

List of Figures

Acknowledgments

Special thanks goes to my advisor, Dr. Elijah Thimsen for academic and research support, as well as the other two members of my committee, Dr. Pratim Biswas and Dr. Bryce Sadtler.

The following thesis has been reprinted with permission from:

> Contact Radius and the Insulator–Metal Transition in Films Comprised of Touching Semiconductor Nanocrystals
> Deanna Lanigan and Elijah Thimsen
> ACS Nano 2016 10 (7), 6744-6752
> DOI: 10.1021/acsnano.6b02190

Deanna Lanigan

Washington University in St. Louis
August 2016

Dedicated to my family.

ABSTRACT OF THE THESIS

Contact Radius and the Insulator-Metal Transition in Films Comprised of Semiconductor

Nanocrystals

by

Deanna Lanigan

Master of Science in Energy, Environmental, and Chemical Engineering

Washington University in St. Louis, 2016

Research Advisor: Dr. Elijah Thimsen

Nanocrystal assemblies are being explored for a number of optoelectronic applications such as transparent conductors, photovoltaic solar cells, and electrochromic windows. Majority carrier transport is important for these applications, yet it remains relatively poorly understood in films comprised of touching nanocrystals. Specifically, the underlying structural parameters expected to determine the transport mechanism have not been fully elucidated. In this report, we demonstrate experimentally that the contact radius, between touching heavily doped ZnO nanocrystals, controls the electron transport mechanism. Spherical nanocrystals are considered, which are connected by a circular area. The radius of this circular area is the contact radius. For nanocrystals that have local majority carrier concentration above the Mott transition, there is a critical contact radius. If the contact radius between nanocrystals is less than the critical value, then the transport mechanism is variable range hopping. If the contact radius is greater than the critical value, the films display behavior consistent with metallic electron transport.

Chapter 1

Introduction

Films comprised of nanocrystals are being explored for applications in which electron transport is imperative to performance. For example, researchers are actively exploring films comprised of nanocrystals for transparent conductors,[1−3] electrochromic windows,[4−6] photovoltaic solar cells,[7−11] and field-effect transistors.[11−13] Nanocrystals may be synthesized by a variety of solution-phase and aerosol processing techniques, increasing the flexibility of manufacturing options.[14,15] From an industrial perspective, films comprised of nanocrystals may be deposited over large areas with fast deposition rates via continuous roll-to-roll processing, inkjet printing, and other low temperature deposition processes for sensitive substrates.[14−17] From a fundamental perspective, the ability to tune nanocrystal properties such as size, surface chemistry, electronic energy levels, and long-range ordering, can be used to verify theoretical results.[15,18]

The study of films comprised of nanocrystals occupies a unique space where applied science and fundamental research interests coincide. Predictive models are desirable because they allow a priori design of nanostructure. However, before they can be accepted, predictive models must be vetted by independent experimental verification. An important phenomenon that we seek to predict is the insulator−metal transition in nanocrystal films as a function of the physical structure, specifically the contact radius.

Chapter 2

The Insulator-Metal Transition

2.1 The Mott Transition

Conductive materials often display an insulator–metal transition (IMT). For bulk materials, the IMT occurs when the majority carrier density passes the well-known Mott transition[19]

$$n_M r_B^3 \approx 0.02 \qquad \text{(eq. 1)}$$

where r_B is the effective Bohr radius and n_M is the critical majority carrier concentration. The effective Bohr radius r_B is a material property, equal to 1.4 nm in ZnO.[3] If $n > n_M$, then the material displays metallic transport; and if $n < n_M$, then the material behaves as an insulator. For a film comprised of nanocrystals to display a metallic transport mechanism, which is often the goal, the local majority carrier density obviously must be greater than the Mott transition. For ZnO, rearrangement of eq 1 and using $r_B = 1.4$ nm yields $n_M = 7.3 \times 10^{18}$ cm^{-3}. However, although $n > n_M$ is necessary, it is an insufficient criterion for metallic transport in films comprised of nanocrystals.

2.2 Contact Resistance and the Insulator-Metal Transition

In many cases, the morphology of the film and connectivity of nanoparticles have been shown to affect the electron transport mechanism,[20-24] and Beloborodov et al. have demonstrated that there is an additional criterion to describe the IMT in films comprised of heavily doped nanocrystals.[25] Specifically, the contact resistance between nanocrystals must be less than the quantum resistance, $R_Q = \hbar/2e^2 = 12.9$ kΩ, for the material to display metallic transport (section I.B of ref 25). If the transport mechanism is metallic, then the resistivity is a very weak function of temperature. If $R_C > R_Q$, then the material behaves as an insulator and the transport mechanism is Efros–Shklovskii variable range hopping. In the insulating regime, the resistivity has the well-known stretched exponential dependence on temperature

$$\rho(T) = \rho_0 exp[(T_0/T)^m] \qquad \text{(eq. 2)}$$

where T_0 and ρ_0 are constants and $m = 1/2$. Thus, the electron transport mechanism in a film comprised of nanocrystals can be determined by measuring the resistivity as a function of temperature. The theory of Beloborodov et al. is powerful because it provides a criterion to predict the transport mechanism in films comprised of heavily doped nanocrystals. However, it is not obvious how the contact resistance is related to underlying structural characteristics, for example nanocrystal size or contact radius. As such, the theoretical result is not straightforward to apply to design the physical structure of a film.

2.3 Contact Area and the Insulator-Metal Transition

More recently, the theory of Beloborodov et al. has been extended by Fu, Reich, and Shklovskii.[26-28] Specifically, for touching nanocrystals, the quasiclassical expression for the resistance of a point contact,[29, 30] which depends on contact radius and doping density, has been equated to the quantum resistance to derive the criterion for the insulator–metal transition as a function of the contact radius and majority carrier concentration.[26] The result is a simple, unambiguous criterion for the insulator–metal transition in terms of the physical structure of the film comprised of nanocrystals[26]

$$n_{crit} r_C^3 \approx 0.3g \qquad \text{(eq. 3)}$$

where n_{crit} is the critical doping density, r_C is the contact radius between particles, and g is the number of equivalent minima in the conduction band, which is 1 for ZnO.[31]

Obviously, n_{crit} must be greater than n_M. One way to use eq 3 is to predict that for a given contact radius, the transport mechanism will change from variable range hopping to metallic transport as n crosses n_{crit}. Chen, Kramer, and Kortshagen have tested eq 3 experimentally by fabricating films comprised of Si nanocrystals with different doping densities, which were assumed to have the same contact radius between particles. The resulting transport characteristics were found to be consistent with eq 3.[26] Equation 3, to our knowledge, has not been independently verified by a group of researchers other than the ones who proposed it. If eq 3 is correct, then if the majority carrier concentration is held constant, the transport mechanism is predicted to change from

variable range hopping to metallic transport as the contact radius becomes larger than $(0.3 \, g/n)^{1/3}$, provided $n > n_M$. To our knowledge, this prediction has not been experimentally tested.

2.4 Objectives

In this work, we study the effect of contact radius on the electron transport mechanism for films comprised of heavily doped ZnO nanocrystals that have $n > n_M$. It has been observed previously that as the interparticle spacing decreases, the longitudinal charge carrier mobility through films comprised of nanocrystals increases.[13, 32, 33] Therefore, in this work, we focus on particles that are abutted against one another; that is, touching nanocrystals. The nanocrystals used in this study were not quantum confined, and the spacing between electron energy levels was less than the kinetic energy, which justifies use of the semiclassical criterion for the IMT (eq 3). Although, we note that it has been argued that the IMT criterion also applies to the quantum-confined case.[26] The contact radius was varied by coating films comprised of 7 nm diameter ZnO nanocrystals with a small, controlled amount of ZnO by atomic layer deposition (ALD). ALD is a layer-by-layer thin film deposition method that allows conformal coatings to be deposited on high surface area substrates, with control over coating thickness at the angstrom length scale.[34]

The contact radius was determined by two independent methods. The first method is based on a geometrical argument. Assuming that the centers of spherical particles stay fixed during the ALD coating process, as the radii increase, a circular contact area is defined where the spheres overlap. The radius of this circular contact area is the contact radius. The second method to calculate the contact radius is based on calculating the contact resistance, using the measured resistivity, by

treating the film comprised of nanocrystals as a random resistor network. If the contact resistance and majority carrier concentration are known, then the contact radius can be calculated using the quasiclassical expression.[27] These two independent methods to calculate the contact radius agree for small numbers of ALD ZnO cycles. It is demonstrated that the ALD process is effective to control the contact radius, and that this microscopic parameter can be estimated *a priori*, as a function of ALD coating thickness, to a reasonable degree of accuracy. By holding the local electron concentration constant at 9×10^{19} cm^{-3} and varying the contact radius from 0.6 to 4 nm, we observe significant changes in the electrical properties that are consistent with the IMT occurring at the value of r_C predicted by eq 3.

Chapter 3

Experimental Procedure

3.1   Fabrication

Samples were prepared by a three-step procedure (Figure 3.1). The first step was deposition of the film comprised of ZnO nanocrystals. The second step was the coating of this film with a small, controlled amount of ZnO by ALD to alter the contact radius. The third step was infilling of the remaining pores in the ZnO film with Al_2O_3, which is necessary to render the film conductive.[3] All parameters in the first and third step were kept constant for each sample. The independent variable was the number of ZnO ALD cycles in the second step, which was used to control the contact radius.

Thin films comprised of ZnO nanocrystals were deposited using nonthermal plasma synthesis and inertial impaction as previously reported.[3] Details can be found in the Methods/Experimental section and the Supporting Information. The films comprised of nanocrystals produced by this gas-phase synthesis process contained no organic ligands, and therefore, the particles were assumed to be touching.
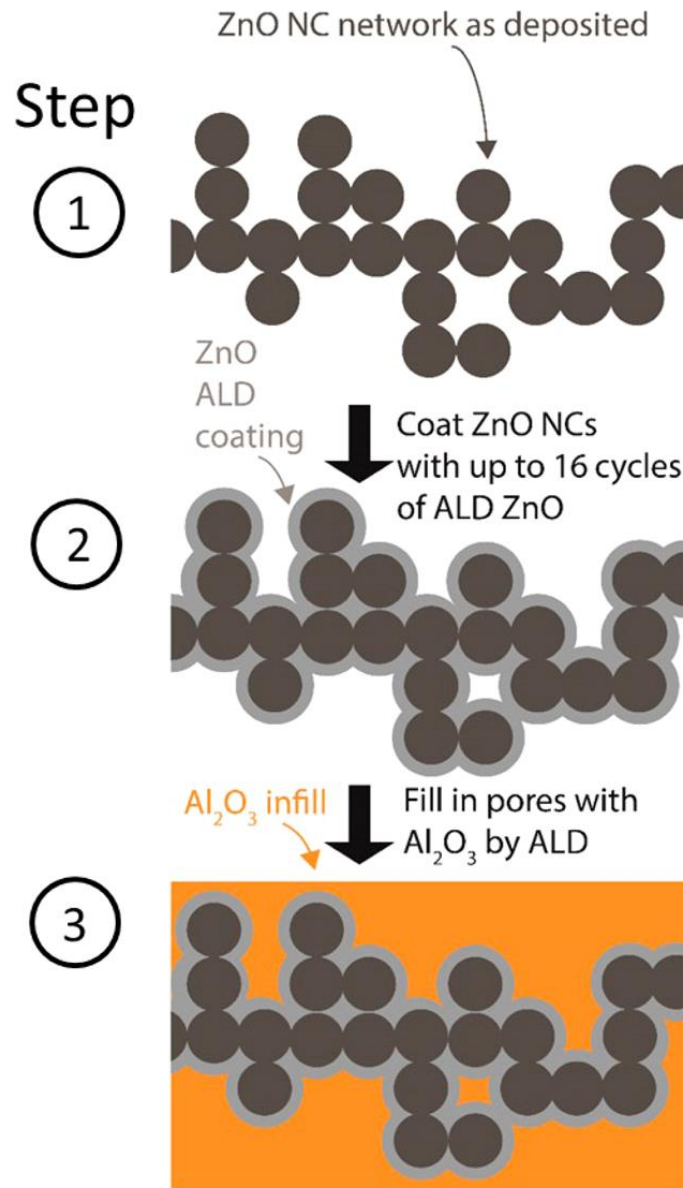
Figure 3.1 Schematic of the nanocrystal network after each of the three processing steps.

3.2   Structural Characterization

As deposited from the plasma reactor, all films used in this study had a thickness in the range from 360 to 430 nm, and a ZnO volume fraction of $\phi(ZnO) = 21 \pm 2\%$ as measured by spectroscopic ellipsometry. A representative cross-sectional scanning electron microscopy (SEM) image of a film deposited on a silicon substrate is presented in Figure 3.2a. The nanocrystals were crystalline zincite, as determined by X-ray diffraction (Supporting Information), with an average diameter of 7 nm, as determined by transmission electron microscopy (TEM) analysis (Figure 3.2b).

The contact radius was modified by coating the film comprised of ZnO nanocrystals with 0 to 16 cycles of ZnO by ALD. At the conditions used in this study, the growth rate per cycle was 0.18 nm. Thus, the thickness of the ALD ZnO coating can be estimated as $d_{ALD} = \eta_{ZnO} \times GPC$, where η_{ZnO} is the number of ALD cycles (0 to 16), and GPC is the growth rate per cycle, which is 0.18 nm cycle^{-1}. TEM images of nanocrystals coated with 4 and 16 cycles of ZnO by ALD are presented in Figure 3.2c and d, respectively. The particles were irregularly shaped, and it is therefore difficult to quantify how the contact radius is changing from the TEM images, but qualitatively, the nanocrystals became more connected. As films comprised of ZnO nanocrystals were coated with ZnO by ALD, the ZnO volume fraction increased, as expected (Figure 32e). However, after coating with ZnO, there still remained a large volume fraction of pores in the film. The pores were filled with Al_2O_3 to remove hydroxyl from the surface of the ZnO.[3]

The remaining pore volume was filled in with Al_2O_3 by ALD, in the third step (Figure 3.1). All samples were coated with 40 cycles of Al_2O_3 by ALD, which was sufficient to fill in the pores

such that the film had greater than 90% solids volume fraction. The deposition of Al_2O_3 on the surfaces of the ZnO nanocrystals rendered the material conductive. The ALD Al_2O_3 process removes acceptor defects from the surfaces of the ZnO nanocrystals, and reduces the ZnO, which decreases the resistivity by approximately 7 orders of magnitude.[3] A full description of the mechanism by which the ALD process decreases the resistivity is out of the scope of the present report and will be presented in a forthcoming publication.
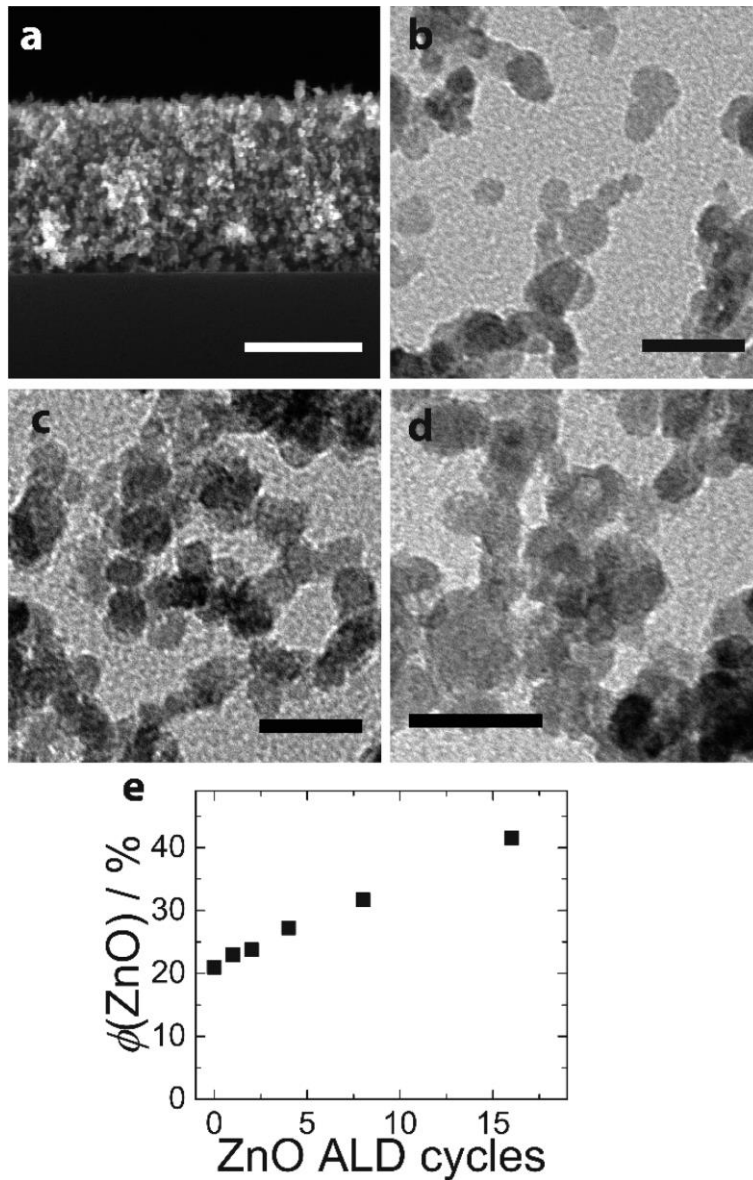
Figure 3.2. Structural characterization. (a) Cross-sectional SEM image of a film comprised of ZnO nanocrystals (NCs) on a silicon substrate that has not been coated by ALD. TEM images of (b) uncoated ZnO NCs, (c) ZnO NCs coated with 4 cycles of ALD ZnO, and (d) ZnO NCs coated with 16 cycles of ALD ZnO. The average size of the NCs in (b) was measured by analyzing several TEM images, and found to be 7 nm. The ZnO volume fraction as a function of the number of ALD ZnO cycles is presented in (e). The scale bar in panel a is 300 nm; in panels b−d, it is 20 nm.

3.3   Electronic Characterization

The free electron concentration in the films comprised of nanocrystals was found to be independent of the number of ZnO ALD cycles (Figure 3.3b). The electron concentration was measured by two independent methods: Fourier transform infrared (FTIR) absorption spectroscopy and Hall effect. For FTIR absorption spectroscopy, films were deposited on single crystal KBr substrates and coated with Al_2O_3 by ALD (Figure 3.3a). The plasmon peak,(1-3) which emerges after coating with Al_2O_3, was fitted using the published model[3] to extract the local carrier concentration and mobility (Figure 3.3a). The local carrier concentration was found to be $n_{local} = 9.0 \times 10^{19}$ cm^{-3} and the local mobility was $\mu_{local} = 10$ cm^2 V^{-1} s^{-1}. Using a carrier concentration of 9.0×10^{19} cm^{-3}, and an average particle radius of 3.5 nm, we estimate that each nanocrystal contains, on average, approximately 16 free electrons.

To verify this result, Hall effect measurements of longitudinal transport were performed at room temperature on samples deposited on glass substrates as a function of ALD ZnO coating thickness (Figure 3.3b). As an aside, we note that samples which had a variable range hopping transport mechanism displayed an anomalous Hall effect below 200 K. Specifically, the Hall coefficient became very large and displayed spatial anisotropy. No anomaly was observed for samples which were synthesized using a large number (8 or 16) of ZnO ALD cycles. At room temperature, for all samples, the Hall coefficient was negative, consistent with electrons as the majority carriers, which is typical of ZnO.[35] The apparent carrier concentration n^* was found to be independent of the ZnO coating thickness (Figure 3.3b).

The apparent carrier concentration by Hall effect was less than the value measured from FTIR absorption spectroscopy, which is expected.[36] For solids comprised of heavily doped nanocrystals, it has been reported that that the apparent carrier concentration measured by Hall effect is equal to the local carrier concentration multiplied by a geometrical factor that is slightly less than 1.[36] As the thickness of the ALD ZnO coating increased, so did the longitudinal mobility as measured by Hall effect (Figure 3.3b). In fact, the mobility measured by Hall effect approached the local mobility measured by FTIR absorption spectroscopy as the particles become well connected (Figure 3.3a,b).

The two primary observations both support the hypothesis that the contact radius is increasing: (1) the electron concentration is independent of the ALD ZnO coating thickness, and (2) the longitudinal mobility increases with increasing ALD ZnO coating thickness. From the electron concentration measured by FTIR absorption spectroscopy (9.0×10^{19} cm^{-3}), and the apparent carrier concentration measured by Hall effect (4×10^{19} cm^{-3}), eq 3 can be used to set the bounds on the contact radius at which the IMT is expected to occur. The IMT is expected to occur in the range: 1.5 nm $< r_C <$ 2.0 nm. The next step is to calculate the contact radius for each of the samples.
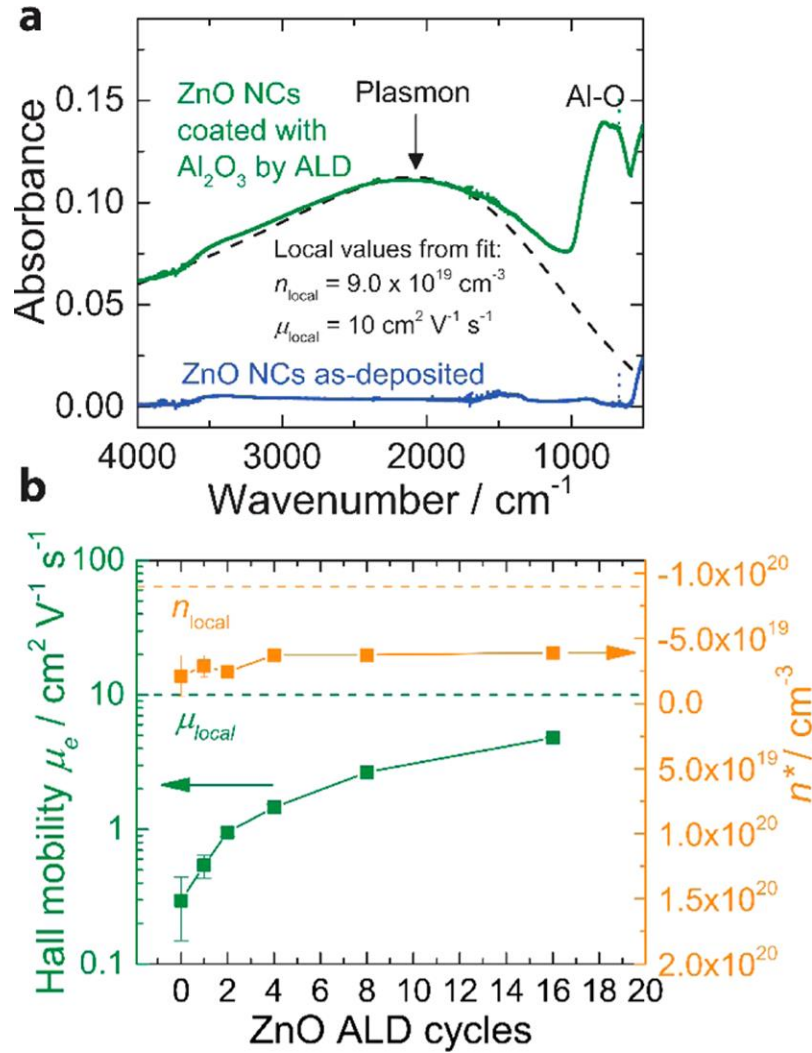
Figure 3.3. Measurement of electron concentration at room temperature. (a) FTIR absorption spectra of (blue) an as-deposited film comprised of ZnO nanocrystals with no ALD coating, and (green) a film comprised of ZnO nanocrystals that have been coated with only 40 cycles of Al2O3 by ALD. The black dashed line in (a) is the fit used to extract the local carrier concentration n_{local} and local mobility μ_{local}. (b) Hall effect measurements of mobility μ_e and apparent carrier concentration n* of films comprised of ZnO nanocrystals that have been coated with different amounts of ZnO by ALD. The horizontal lines in (b) correspond to the values extracted from (a). The error bars in (b) correspond to the standard deviation of 10 measurements of each sample.

14

Chapter 4

Calculation of Contact Radius

Two independent methods are presented to calculate the contact radius between nanocrystals. The first is based on a simple geometrical argument. The second method involves extracting the contact resistance, and then using the quasiclassical expression for contact resistance to calculate the contact radius.

4.1 Geometrical Method

The first method to calculate the contact radius is based on a simple geometrical model, which is illustrated in Figure 4.1. Specifically, we propose that the ZnO nanocrystals can be treated as spheres with a fixed position. As ZnO is deposited on the ZnO nanocrystals, the radii of the spheres will increase. Therefore, the spheres will overlap. The circular region defined by the intersection of the spheres is the contact area. The radius of the contact area is the contact radius. For thin ALD coatings, it can be shown that

$$r_C = \sqrt{d_{ALD}^2 + 2r_0 d_{ALD}} \qquad \text{(eq. 4)}$$

where r_C is the contact radius, r_0 is the initial radius of the nanocrystals as produced by the plasma reactor, which is 3.5 nm, and d_{ALD} is the thickness of the ALD coating.

Equation 4 should be applied cautiously, because for large d_{ALD} the pores in the film will become

filled in, [3] and therefore the model based on unencumbered growth illustrated in Figure 4.1 is no

longer reasonable. At large d_{ALD}, the geometric model will provide the upper limit for the contact

radius. Furthermore, for the case where $d_{ALD}= 0$, eq. 4 does not accurately calculate the contact

radius. In the case where $d_{ALD} = 0$, the contact radius is more accurately described by a b contact,

$r_C(d_{ALD} = 0) = \sqrt{r_0 b}$, where b is the decay length of an electron in the medium surrounding the

nanocrystals, which depends on the work function, and r_0 is the particle radius.(26) Using a work

function of 4.7 eV for Al_2O_3,[37] b is approximately 0.1 nm, and therefore $r_C(d_{ALD} = 0) \approx 0.6$ nm.

Thus, the contact radius can be calculated as a function of experimental conditions and the

measured particle radius, r_0. This method for calculating the contact radius is termed the

geometrical method.
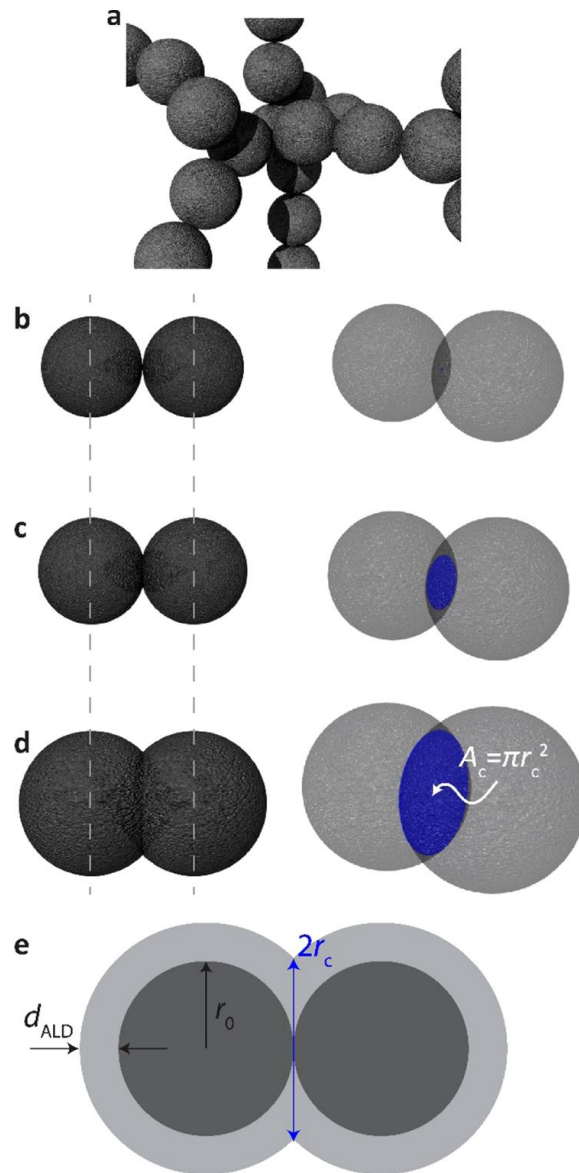
Figure 4.1. Geometrical method. Nanocrystals are treated as spheres that have fixed positions and begin to overlap as the radii increase with ALD coating. (a) Schematic representation of the nanocrystal network. (b–c) Overlap between spheres increases as the ALD coating thickness increases, which increases the contact area AC. (e) Definitions of different geometrical dimensions, d_{ALD} is the ALD coating thickness, r_0 is the initial particle radius as-deposited from the plasma reactor, and r_C is the contact radius.

4.2 Electronic Method

A second independent method is proposed to calculate the contact radius, wherein the film comprised of nanocrystals is envisioned as a random resistor network (RRN) (Figure 4.2.1a). If it is assumed that the RRN is on a cubic three-dimensional lattice, then the lattice constant is equal to the initial distance between the centers of nanocrystals, which is simply the nanocrystal diameter in the as-deposited state (i.e., $2r_0$). We note that in our films the ZnO volume fraction is in the range from 20 to 40% (Figure 3.2e). This can be envisioned as a fractional occupancy of sites on the cubic lattice. In other words, we account for a conducting phase volume fraction less than 1 by allowing a fraction of bonds on the RRN to be broken. The resistors connecting nodes on the lattice have a resistance R_{bond} (Figure 4.2.1a). The bond resistance is

$$R_{bond} = R_0 + R_C \qquad \text{(eq. 5)}$$

where R_0 is the resistance of a single nanocrystal, and R_C is the contact resistance between two nanocrystals (Figure 4.2.1b). The contact resistance of a single particle, R_0, can be calculated if the local mobility, carrier concentration, and size are known (see Supporting Information). The bond resistance can be determined using the links-nodes model.[38-40] From the links-nodes model in three dimensions, the bond resistance in the RRN can be calculated as

$$R_{bond} = \frac{\rho \cdot (\phi - \phi_0)^{1.9}}{2r_0} \qquad \text{(eq. 6)}$$

where ρ is the electrical resistivity of the film comprised of nanocrystals, ϕ is the conducting phase volume fraction (i.e., the ZnO volume fraction) and ϕ_0 is the percolation threshold. In eq. 6, it has been assumed that the probability of a bond on the RRN being occupied is equal to the conducting phase volume fraction. The percolation threshold was determined experimentally to be 5% (Supporting Information). This experimentally measured value for the percolation threshold is less than theoretical values predicted for random bond occupancy on cubic lattices.[40, 41] In films comprised of nanocrystals deposited by ballistic impaction, the particles are self-supporting, and as a result the percolation threshold can be as small as 0.4%.[42] Detailed geometrical descriptions of films comprised of nanocrystals deposited by ballistic impaction can be found in the literature.[42-44]

Because the ZnO volume fraction is known for each sample (Figure 3.2e), the bond resistance can be calculated from the measured resistivity using eq. 6. Once the bond resistance is known, then the contact resistance can be calculated using eq. 5. The contact resistance as a function of the number of ZnO ALD cycles is presented in Figure 4.2.2. The contact resistance decreases with increasing number of ZnO ALD cycles, and crosses the quantum resistance at approximately 2 cycles. Given the contact resistance, the contact radius can be calculated using the quasiclassical expression[26]

$$r_C = \sqrt{\frac{4\pi h}{R_C e^2 k_F^2}} \qquad \text{(eq. 7)}$$

where R_C is the contact resistance (Figure 4.2.2), and k_F is the Fermi wave vector, which can be calculated as

$$k_F = \left(\frac{3\pi^2}{g}n\right)^{1/3} \qquad\qquad \text{(eq. 8)}$$

where n is the electron concentration in a nanocrystal (9.0×10^{19} cm^{-3}) and $g = 1$ for ZnO.

Thus, R_C can then be inserted into eq. 7 to calculate the contact radius, r_C. This method for calculating the contact radius is termed the electronic method.
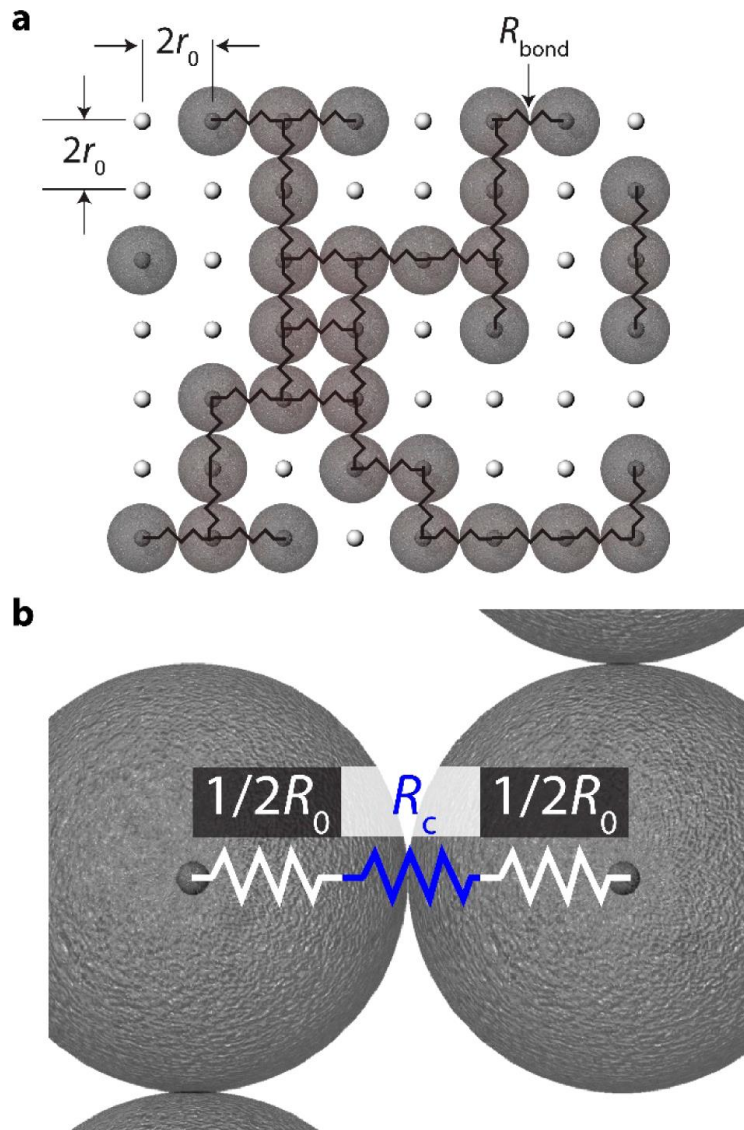
Figure 4.2.1. Electrical method. (a) Random resistor network on a cubic lattice with lattice constant equal to the particle diameter. Conducting phase volume fraction less than unity is accounted for by fractional occupancy of bonds on the random resistor network. (b) Schematic description of one resistor in the random resistor
network.
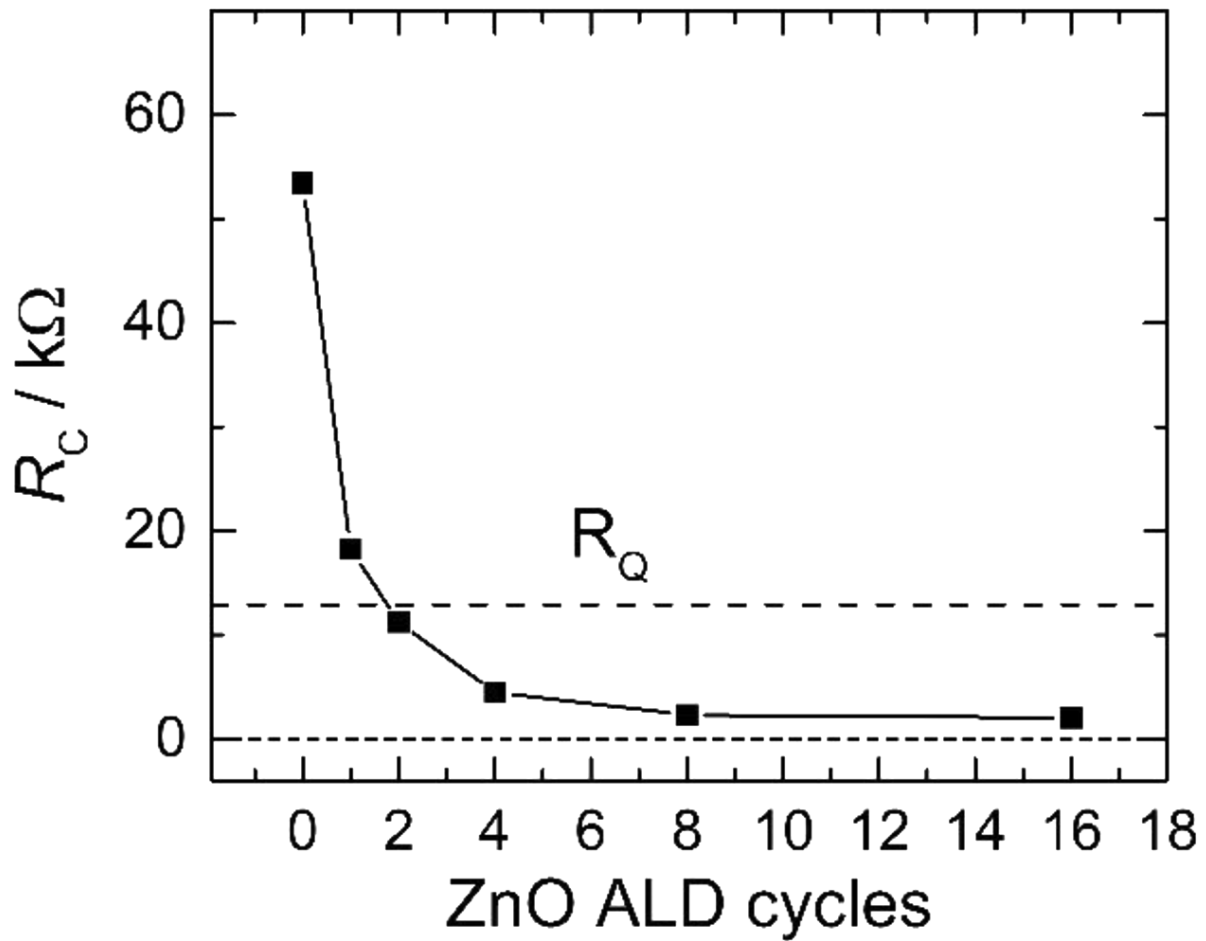
Figure 4.2.2. Interparticle contact resistance as a function of the number of ALD ZnO cycles. R_Q is the quantum resistance.

4.3   Comparison

The two methods for calculating the contact radius agree very well for all samples except the 16 cycle case. In Figure 4.3, the contact radius, calculated using the electronic method from eq. 7, is plotted as a function of the contact radius calculated using the geometrical method from eq. 4. For the 16 cycle case, the geometrical method overestimates the contact radius compared to the electrical method. This discrepancy is hypothesized to be a result of pores of the film being filled, which suppresses the growth of the contact area compared to the ideal unencumbered growth illustrated in Figure 4.1. We surmise that the geometrical method is most accurate for situations in which the coating thickness is much smaller than the characteristic size of the pores in the film comprised of nanocrystals. This condition is apparently valid for 0 to 8 cycles of ZnO ALD but is violated in the 16 cycle case. For ALD cycles greater than 8, the geometric model is the upper limit for the contact radius.

As the ALD coating thickness increases, the discrepancy between models increases. In the real system, new contacts are being created as the pores close. The links–nodes model (electrical method) can account for the formation of new small connections as pores close, but the geometrical method cannot. The new contacts will have a smaller contact radius than the value predicted by the geometric model. However, because the current will flow along the path of least resistance, these new contacts are not expected to affect the transport mechanism. Having reliable estimates for the contact radius for each of the samples, the criterion given in eq. 3 can now be verified by determining the transport mechanism.
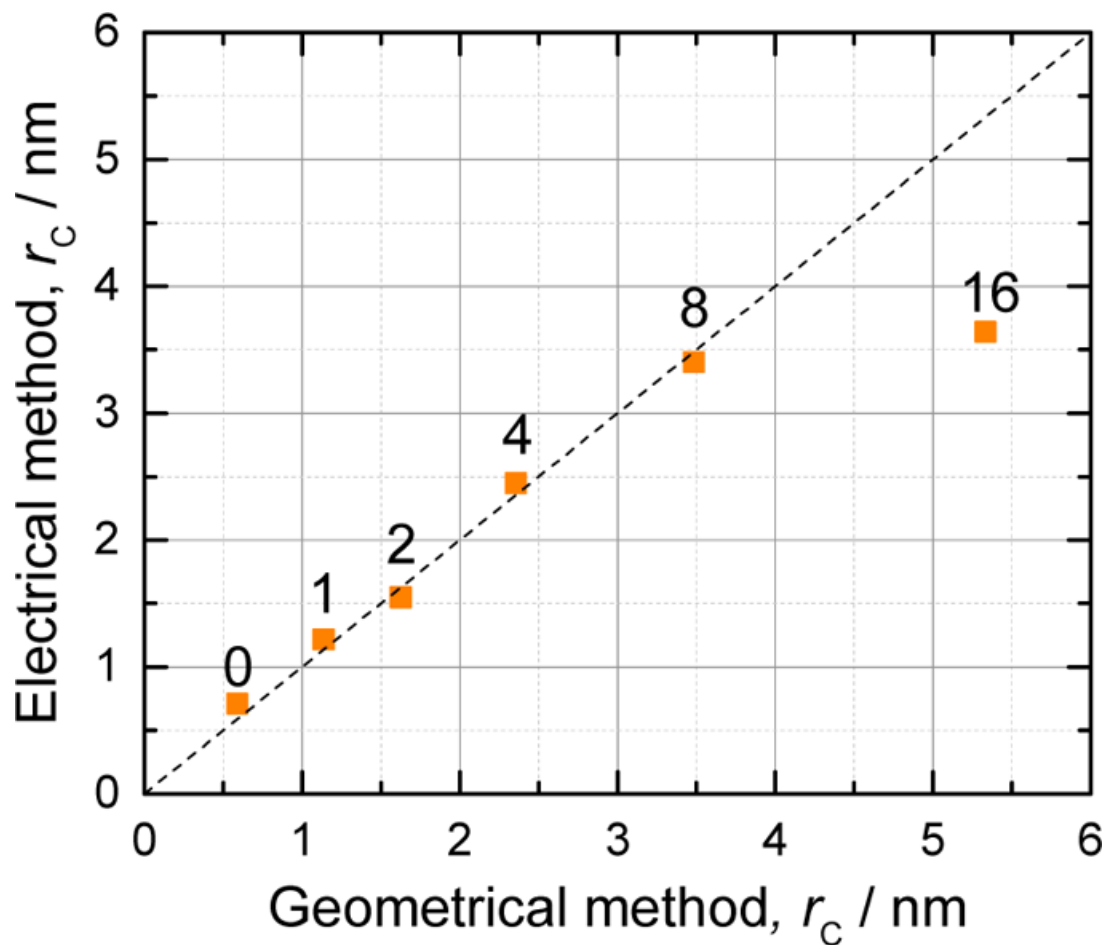
Figure 4.3. Contact radius determined by the electrical method plotted as a function of contact radius determined by the geometrical method for different numbers of ZnO ALD cycles. The number of ZnO ALD cycles used to synthesize each sample is the number above the symbol.

Chapter 5

Determination of Transport Mechanism

The IMT is expected to occur for a contact radius in the range from 1.5 to 2.0 nm, as described above. The contact radius is less than 1.5 nm for both 0 and 1 cycles of ALD ZnO (Figure 4.3), and therefore, a variable range hopping (VRH) transport mechanism is expected for these samples. The contact radius is approximately equal to the IMT critical radius for the 2 and 4 cycle cases, and thus, these samples are expected to be in the transition regime between insulator and metallic. The contact radius is significantly larger than 2.0 nm for both 8 and 16 cycles of ALD ZnO, and therefore, a metallic transport mechanism is expected. Measurements of the resistivity as a function of temperature in the range from 7 to 300 K were performed to determine the transport mechanism.

Consistent with the prediction of eq 3, both the 0 and 1 cycle cases exhibited a VRH transport mechanism. Plotted in Figure 5a is the measured resistivity as a function of temperature and ZnO ALD cycles. The 0 and 1 cycle cases exhibit a stretched exponential dependence of the resistivity on temperature over the entire temperature range. It was found that $m = 1/2$ (eq. 2) from Zabrodskii analysis[45] performed on the data in Figure 5a (not shown here). Thus, the transport mechanism was Efros-Shklovskii variable range hopping (ES-VRH). The characteristic temperature, T_0, was extracted from the slope of the plot of $\ln(\rho)$ as a function of $T^{-1/2}$, which is

nominally linear over the entire temperature range investigated here (Figure 5b). For ES-VRH, in SI units, T_0 is related the electron localization length by

$$T_0 = \frac{Be^2}{4\pi\varepsilon k_B \xi}$$ (eq. 9)

where B is a numerical constant in the range from 2.8 to 9.6 in 3D,(21, 46) which we assume here to be 9.6, ε is the dielectric constant of the film, k_B is the Boltzmann constant and ξ is the electron localization length. The dielectric constant can be calculated from the Maxwell–Garnett formula[47] using the measured ZnO volume fraction (Figure 3.2e), considering ZnO inclusions in an Al_2O_3 matrix. The dielectric constant is estimated to be $\varepsilon \approx 8.8\varepsilon_0$. The localization length is large. In the 0 cycle case it is approximately 31 nm, and in the 1 cycle case, it is 64 nm. Such large localization lengths indicate that the material is approaching the IMT.[26]

The temperature dependence of the resistivity for the 8 and 16 cycle samples was very weak (Figure 5a). Materials displaying metallic transport have finite resistivity at 0 K. The minimum temperature at which we performed measurements was 7 K. It is impossible to perform measurements at 0 K using current experimental procedures; however, a reasonable extrapolation to 0 K would result in finite resistivity. The carrier concentration measured by Hall effect was found to be independent of temperature (Figure 5c), which again is consistent with metallic transport. Therefore, these results are consistent with the prediction of eq 3 that the IMT occurs at a contact radius of approximately 2 nm.
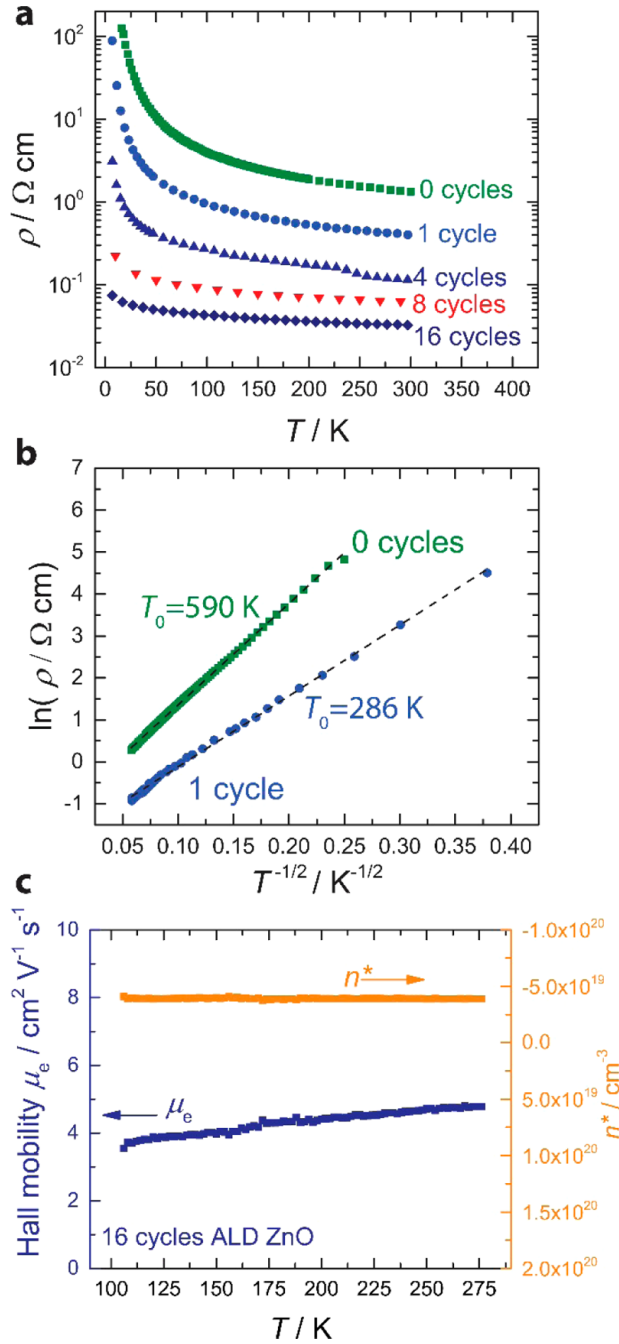
Figure 5. Transport mechanism. (a) Resistivity as a function of temperature and number of ZnO ALD. (b) Plot demonstrating that $\ln(\rho)$ is linear with respect to $T^{-1/2}$, consistent with the value of $m = 1/2$ determined from Zabrodskii analysis. (c) Carrier concentration measured by Hall effect is independent of temperature, consistent with metallic transport.

27

Chapter 6

Conclusion

In this work, we experimentally explored the recently proposed criterion for the IMT in films comprised of touching, heavily doped semiconductor nanocrystals.[26-28] All samples reported here had nominally the same electron concentration, as determined by FTIR absorption spectroscopy and Hall effect measurements. Each sample had a different value for the interparticle contact radius, in the range from 0.6 to 4 nm. The results are consistent with, but do not provide a complete proof of, the IMT occurring at the contact radius predicted by eq. 3.

References

(1) Buonsanti, R.; Llordes, A.; Aloni, S.; Helms, B. A.; Milliron, D. J. Tunable Infrared Absorption and Visible Transparency of Colloidal Aluminum-Doped Zinc Oxide Nanocrystals. Nano Lett. 2011, 11, 4706−4710.

(2) Greenberg, B. L.; Ganguly, S.; Held, J. T.; Kramer, N. J.; Mkhoyan, K. A.; Aydil, E. S.; Kortshagen, U. R. Nonequilibrium- Plasma-Synthesized ZnO Nanocrystals with Plasmon Resonance Tunable via Al Doping and Quantum Confinement. Nano Lett. 2015, 15, 8162−8169.

(3) Thimsen, E.; Johnson, M.; Zhang, X.; Wagner, A. J.; Mkhoyan, K. A.; Kortshagen, U. R.; Aydil, E. S. High Electron Mobility in Thin Films Formed via Supersonic Impact Deposition of Nanocrystals Synthesized in Nonthermal Plasmas. Nat. Commun. 2014, 5, 5822.

(4) Kim, J.; Ong, G. K.; Wang, Y.; LeBlanc, G.; Williams, T. E.; Mattox, T. M.; Helms, B. A.; Milliron, D. J. Nanocomposite Architecture for Rapid, Spectrally-Selective Electrochromic Modulation of Solar Transmittance. Nano Lett. 2015, 15, 5574−5579.

(5) Llordes, A.; Garcia, G.; Gazquez, J.; Milliron, D. J. Tunable Near- Infrared and Visible-Light Transmittance in Nanocrystal-in-Glass Composites. Nature 2013, 500, 323−326.

(6) Runnerstrom, E. L.; Llordes, A.; Lounis, S. D.; Milliron, D. J. Nanostructured Electrochromic Smart Windows: Traditional Materials and NIR-Selective Plasmonic Nanocrystals. Chem. Commun. 2014, 50, 10555−10572.

(7) Semonin, O. E.; Luther, J. M.; Choi, S.; Chen, H. Y.; Gao, J. B.; Nozik, A. J.; Beard, M. C. Peak External Photocurrent Quantum Efficiency Exceeding 100% via MEG in a Quantum Dot Solar Cell. Science 2011, 334, 1530−1533.

(8) Kramer, I. J.; Sargent, E. H. Colloidal Quantum Dot Photovoltaics: A Path Forward. ACS Nano 2011, 5, 8506−8514.

(9) Chernomordik, B. D.; Béland, A. E.; Deng, D. D.; Francis, L. F.; Aydil, E. S. Microstructure Evolution and Crystal Growth in Cu2ZnSnS4 Thin Films Formed By Annealing Colloidal Nanocrystal Coatings. Chem. Mater. 2014, 26, 3191−3201.

(10) Crisp, R. W.; Panthani, M. G.; Rance, W. L.; Duenow, J. N.; Parilla, P. A.; Callahan, R.; Dabney, M. S.; Berry, J. J.; Talapin, D. V.; Luther, J. M. Nanocrystal Grain Growth and Device Architectures for High-Efficiency CdTe Ink-Based Photovoltaics. ACS Nano 2014, 8, 9063−9072.

(11) Liu, Y.; Tolentino, J.; Gibbs, M.; Ihly, R.; Perkins, C. L.; Liu, Y.; Crawford, N.; Hemminger, J. C.; Law, M. PbSe Quantum Dot Field- Effect Transistors with Air-Stable Electron Mobilities above 7 cm(2) V-1 s(−1). Nano Lett. 2013, 13, 1578−1587.

(12) Choi, J. H.; Fafarman, A. T.; Oh, S. J.; Ko, D. K.; Kim, D. K.; Diroll, B. T.; Muramoto, S.; Gillen, J. G.; Murray, C. B.; Kagan, C. R. Bandlike Transport in Strongly Coupled and Doped Quantum Dot Solids: A Route to High-Performance Thin-Film Electronics. Nano Lett. 2012, 12, 2631−2638.

(13) Lee, J.-S.; Kovalenko, M. V.; Huang, J.; Chung, D. S.; Talapin, D. V. Band-like Transport, High Electron Mobility and High Photoconductivity in All-Inorganic Nanocrystal Arrays. Nat. Nanotechnol. 2011, 6, 348−352.

(14) Kruis, F. E.; Fissan, H.; Peled, A. Synthesis of Nanoparticles in the Gas Phase for Electronic, Optical and Magnetic Applications: a review. J. Aerosol Sci. 1998, 29, 511−535.

(15) Talapin, D. V.; Lee, J.-S.; Kovalenko, M. V.; Shevchenko, E. V. Prospects of Colloidal Nanocrystals for Electronic and Optoelectronic Applications. Chem. Rev. 2010, 110, 389−458.

(16) Shipway, A. N.; Katz, E.; Willner, I. Nanoparticle Arrays on Surfaces for Electronic, Optical, and Sensor Applications. ChemPhysChem 2000, 1, 18−52.

(17) Dasgupta, S.; Kruk, R.; Mechau, N.; Hahn, H. Inkjet Printed, High Mobility Inorganic-Oxide Field Effect Transistors Processed at Room Temperature. ACS Nano 2011, 5, 9628−9638.

(18) Whitham, K.; Yang, J.; Savitzky, B. H.; Kourkoutis, L. F.; Wise, F.; Hanrath, T. Charge Transport and Localization in Atomically Coherent Quantum Dot Solids. Nat. Mater. 2016, 15, 557.

(19) Mott, N. F. Metal-Insulator Transition. Rev. Mod. Phys. 1968, 40, 677.

(20) Sandeep, C. S. S.; Azpiroz, J. M.; Evers, W. H.; Boehme, S. C.; Moreels, I.; Kinge, S.; Siebbeles, L. D. A.; Infante, I.; Houtepen, A. J. Epitaxially Connected PbSe Quantum-Dot

Films: Controlled Neck Formation and Optoelectronic Properties. ACS Nano 2014, 8, 11499− 11511.

(21) Liu, H.; Pourret, A.; Guyot-Sionnest, P. Mott and Efros- Shklovskii Variable Range Hopping in CdSe Quantum Dots Films. ACS Nano 2010, 4, 5211−5216.

(22) Zhang, X.; Manno, M.; Baruth, A.; Johnson, M.; Aydil, E. S.; Leighton, C. Crossover From Nanoscopic Intergranular Hopping to Conventional Charge Transport in Pyrite Thin Films. ACS Nano 2013, 7, 2781−2789.

(23) Norman, Z. M.; Anderson, N. C.; Owen, J. S. Electrical Transport and Grain Growth in Solution-Cast, Chloride-Terminated Cadmium Selenide Nanocrystal Thin Films. ACS Nano 2014, 8, 7513−7521.

(24) Li, H.; Zhitomirsky, D.; Dave, S.; Grossman, J. C. Toward the Ultimate Limit of Connectivity in Quantum Dots with High Mobility and Clean Gaps. ACS Nano 2016, 10, 606−614.

(25) Beloborodov, I. S.; Lopatin, A. V.; Vinokur, V. M.; Efetov, K. B. Granular Electronic Systems. Rev. Mod. Phys. 2007, 79, 469−518.

(26) Chen, T.; Reich, K. V.; Kramer, N. J.; Fu, H.; Kortshagen, U. R.; Shklovskii, B. I. Metal-insulator Transition in Films of Doped Semiconductor Nanocrystals. Nat. Mater. 2015, 15, 299.

(27) Fu, H.; Reich, K. V.; Shklovskii, B. I. Hopping Conductivity and Insulator-Metal Transition in Films of Touching Semiconductor Nanocrystals. Phys. Rev. B: Condens. Matter Mater. Phys. 2016, 93, 125430.

(28) Reich, K. V.; Shklovskii, B. I. Dielectric Constant and Charging Energy in Array of Touching Nanocrystals. Appl. Phys. Lett. 2016, 108, 113104.

(29) Sharvin, Y. V. A Possible Method for Studying Fermi Surfaces. Sov. Phys. JETP 1965, 21, 655.

(30) Nikolic, B.; Allen, P. B. Electron Transport Through a Circular Constriction. Phys. Rev. B: Condens. Matter Mater. Phys. 1999, 60, 3963−3969.

(31) Madelung, O. Semiconductors: Basic Data, 2nd ed.; Springer: Berlin/New York, 1996; p 317

(32) Liu, Y.; Gibbs, M.; Puthussery, J.; Gaik, S.; Ihly, R.; Hillhouse, H. W.; Law, M. Dependence of Carrier Mobility on Nanocrystal Size and Ligand Length in PbSe Nanocrystal Solids. Nano Lett. 2010, 10, 1960−1969.

(33) Kovalenko, M. V.; Scheele, M.; Talapin, D. V. Colloidal Nanocrystals with Molecular Metal Chalcogenide Surface Ligands. Science 2009, 324, 1417−1420.

(34) George, S. M. Atomic Layer Deposition: An Overview. Chem. Rev. 2010, 110, 111−131.

(35) Ozgur, U.; Alivov, Y. I.; Liu, C.; Teke, A.; Reshchikov, M. A.; Dogan, S.; Avrutin, V.; Cho, S. J.; Morkoc, H. A Comprehensive Review of ZnO Materials and Devices. J. Appl. Phys. 2005, 98, 041301.

(36) Kharitonov, M. Y.; Efetov, K. B. Hall Resistivity of Granular Metals. Phys. Rev. Lett. 2007, 99, 056803.

(37) Fomenko, V. S.; Samsonov, G. V. Handbook of Thermionic Properties; Electronic Work Functions and Richardson Constants of Elements and Compounds; Plenum Press Data Division Consultants Bureau Enterprises: New York, 1966; p vii, 151 pp.

(38) Skal, A. S.; Shklovskii, B. I. Topology of an Infinite Cluster in Theory of Percolation and Its Relationship to Theory of Hopping Conduction. Sov. Phys. Semicond. 1975, 8,1029−1032.

(39) De Gennes, P. G. On a Relation Between Percolation Theory and the Elasticity of Gels. J. Phys., Lett. 1976, 37, 1−2.

(40) Shklovskii, B. I.; Efros, A. L. Electronic Properties of Doped Semiconductors. Springer-Verlag: Berlin ; New York, 1984; p xii, 388 p.

(41) Stauffer, D.; Aharony, A. Introduction to Percolation Theory, 2nd ed.; Taylor & Francis: London/Washington, DC, 1992; p x, 181 pp.

(42) Riefler, N.; Madler, L. Structure-Conductivity Relations of Simulated Highly Porous Nanoparticle Aggregate Films. J. Nanopart. Res. 2010, 12, 853−863.

(43) Kulkarni, P.; Biswas, P. A Brownian Dynamics Simulation to Predict Morphology of Nanoparticle Deposits in the Presence of Interparticle Interactions. Aerosol Sci. Technol. 2004, 38, 541−554.

(44) Madler, L.; Lall, A.; Friedlander, S. One-Step Aerosol Synthesis of Nanoparticle Agglomerate Films: Simulation of Film Porosity and Thickness. Nanotechnology 2006, 17, 4783−4795.

(45) Zabrodskii, A. G. The Coulomb Gap: the View of an Experimenter. Philos. Mag. B 2001, 81, 1131−1151.

(46) Skinner, B.; Chen, T.; Shklovskii, B. I. Theory of Hopping Conduction in Arrays of Doped Semiconductor Nanocrystals. Phys. Rev. B: Condens. Matter Mater. Phys. 2012, 85, 205316.

(47) Maxwell, J. C. A Treatise on Electricity and Magnetism; Clarendon Press: Oxford, U.K., 1881; Vol. 1.

(48) Holman, Z. C.; Kortshagen, U. R. A Flexible Method for Depositing Dense Nanocrystal Thin Films: Impaction of Germanium Nanocrystals. Nanotechnology 2010, 21, 335302.

Appendix A

Methods/Experimental

Thin films comprised of ZnO nanocrystals (NCs) were deposited with controlled interparticle contact resistance by a three step procedure (Figure 3.1). Detailed parameters of the plasma reactor and atomic layer deposition can be found in the Supporting Information.

The first step was synthesis of ZnO NCs in the gas phase by reacting a mixture of argon, diethyl zinc (DEZ), and O_2 in a radiofrequency plasma using a reactor that is similar to the one previously reported.[3] The main difference was that the pressure in the impaction stage was 0.55 Torr. Downstream of the plasma, the ZnO NC aerosol was expanded through a nozzle to supersonic velocity and impinged on a deposition substrate that was placed in the particle beam. Silicon substrates were used for structural characterization, glass substrates where used for electrical measurements, and KBr was used for infrared absorption. The ZnO particles, which acquire very high velocity (100s of m s^{-1}) in the nozzle,[48] deposited on the substrates by inertial impaction. The substrates were moved back and forth under the beam in a reciprocating motion to simulate a roll-to-roll deposition process, and thereby a film comprised of ZnO NCs was deposited.

The second step of the procedure was to coat the ZnO NC network with a small controlled amount of ZnO by ALD, from 0 to 16 cycles (Figure 3.1). This parameter is the independent variable in the experiment. Each cycle of ALD deposited nominally 0.18 nm of ZnO on the

surface of the nanoparticles. Detailed ALD conditions can be found inSupporting Information.

Under these conditions, the ALD precursor gases penetrate almost completely into the voids of

the porous nanoparticle film. For example, if enough ALD cycles were carried out to completely

fill the voids (~40 cycles at 1.1 Å cycle^{-1} for the geometries explored herein), the measured

solids volume fraction increased from 21% initially to approximately 98% after ALD coating;

while overall film thickness did not change significantly. Detailed electron microscopy that

further proves this point can be found in previous work.[3]

In the third step, all samples were coated with the same number of ALD Al_2O_3 cycles (40

cycles), which was sufficient to fill in the accessible voids. The Al_2O_3 infilling results in a thin

overcoat of Al_2O_3, but it is assumed there is no resulting effect on the four-point electrical

characterization subsequently performed. In summary, films comprised of ZnO nanocrystals

were deposited with nominally the same particle size, film thickness and solid volume fraction.

These films were coated with variable amounts of ZnO by ALD, and then all films were filled in

using the same number of Al_2O_3 cycles.

Material characterization was performed by a variety of techniques. For scanning electron

microscopy (SEM), ZnO nanocrystals were deposited on silicon substrates. These substrates

were scored using a diamond scribe, and then cleaved to produce a sharp edge. The samples were

then mounted in a 90° holder so the cross section could be imaged. Electron micrographs were

acquired using an FEI Nova NanoSEM 230 field emission microscope operating at 3 kV

accelerating voltage.

Samples were prepared on transmission electron microscopy (TEM) specimen supports by mounting the copper grids to the sample holder in the plasma reactor. The copper grids contained an electron-transparent lacey carbon layer for mechanical support and a 3 nm continuous carbon layer to support the particles. ZnO nanocrystals were deposited on the specimen support for approximately 1 s so the particle layer was electron transparent. These specimens were coated with variable amounts of ZnO by ALD as indicated in the text. Images were acquired using an FEI Tecnai G2 Spirit TEM with a thermal emission gun operating at an accelerating voltage of 120 kV.

Ellipsometry was carried out using an α-SE spectroscopic ellipsometer (J. A. Woolam, Lincoln, NE) in the wavelength range from 380 to 900 nm. The resulting spectra were fit using a Bruggeman effective medium approximation to extract the film thickness and ZnO volume fraction. FTIR spectroscopy was carried out using Nicolette Nexus 470 operating in transmission mode. Single crystal KBr substrates were used for FTIR spectroscopy. The spectra were baseline subtracted using a blank KBr substrate.

Electrical characterization was performed using two different apparatuses. The sample contact pads were metallic indium. Hall effect measurements were performed using an Ecopia HMS-5000 using the van der Pauw electrode configuration. The magnetic field was constant at 0.542 T. This field was applied in both the positive and negative direction so effects of magnetoresistance could be canceled out. For each magnetic field direction, the Hall coefficient was measured along the AC diagonal and the BD diagonal using both positive and negative current. The results of these eight measurements were averaged for each reported Hall coefficient. Measurements under magnetic field were compared to measurements using the same

conditions with no magnetic field to ensure that adequate signal-to-noise ratio was achieved. The

working current was varied in the range from 10 to 200 μA depending on the sample resistivity.

Measurements of resistance as a function of temperature were performed in a Physical Property

Measurement System (PPMS) in the Center for Nanoscale Materials at Argonne National

Laboratory. Measurements were made using a standard four-point electrode configuration with

connections prepared using a wire bonder. The working current was in the range from 1 to 100

μA depending on the sample resistance. The temperature was allowed to stabilize at each point

before taking a measurement. The working current was only applied during resistance

measurement, and was turned off during temperature ramp between points.

Appendix B

Supplementary Information

Plasma Reactor and Atomic Layer Deposition.

Films comprised of ZnO NCs were deposited using a reactor similar to the one previously described.[1] The plasma reactor consisted of fused silica tube, 19 mm outer diameter and 17 mm inner diameter. Three gas streams were combined and passed through the fused silica tube. Flows of argon and oxygen were controlled using mass flow controllers (GE50A, MKS Instruments). The first stream was a flow of oxygen at 30 standard cubic centimeters per minute (SCCM). The second stream was a flow of pure argon at a rate of 300 SCCM. The third stream was a flow of 30 SCCM of argon that was passed through a bubbler containing diethyl zinc (DEZ) at room temperature and a total pressure of 100 Torr before being passed through the reactor. It was assumed that this stream became saturated with DEZ and therefore the feed rate of DEZ was estimated to be 4 SCCM. The total pressure in the quartz tube during reaction was 16 Torr. Thus the partial pressures of argon, oxygen and DEZ in the feed gas were estimated to be 14.5 Torr, 1.3 Torr and 0.2 Torr respectively. A plasma was generated in the quartz tube by applying a radiofrequency (RF) signal at 13.56 MHz through a custom impedance matching network to two copper rings wrapped around the fused silica tube that served as electrodes. In the direction of flow, the electrode rings were 1 centimeter long and separated by a 1 centimeter gap. The forward power displayed on the RF power supply was 60 W. The DEZ and O_2 reacted in the plasma to form ZnO NCs. The aerosol was accelerated through a nozzle that was 0.8 mm x 20 mm, and 67 mm long in the direction of flow. The pressure on the downstream side of this

nozzle was 0.55 Torr, and thus the pressure ratio across the nozzle was 29 and the flow was choked. Films were deposited for 45 seconds by moving the substrates (silicon, corning eagle XG or single crystal KBr) back and forth under the particle beam in a reciprocating motion. The deposition rate was approximately 9 nm s^{-1}.

Atomic layer deposition was carried out in a custom hot wall reactor controlled by a computer program. The reactor consisted of a stainless steel tube, which served as a sample compartment, placed in a tube furnace. The sample compartment was maintained at a temperature of 180 ℃ for all experiments in this report. Nitrogen was used as the purge and carrier gas at a constant flow of 30 SCCM throughout the deposition period. The steady state pressure in the reactor with no precursors present was 0.12 Torr. Water was used as the oxygen precusor, trimethyl aluminum (TMA) as the aluminum precursor and DEZ as the zinc precursor. All precursors were maintained at room temperature in stainless steel 50 milliliter Swagelok cylinders. The precursor manifold was maintained at 130 ℃ to preheat the gasses and prevent condensation. Precursor was fed into the reactor by opening a pneumatic valve on a given cylinder for a specified amount of time and relying on the pressure differential, between vapor pressure in the cylinder and the lower pressure in the reactor, to feed the volatile chemical into the sample compartment. The timing sequence for one cycle of ZnO or Al_2O_3 deposition was the same: 0.5 second water dose, followed by 60 second N_2 purge, followed 0.5 second metalorganic dose (either TMA or DEZ), followed by 60 second N_2 purge. Using these parameters, the measured growth rate per cycle by ellipsometry on optically polished silicon wafers was 1.1 Å cycle^{-1} for Al_2O_3 and 1.8 Å cycle^{-1} for ZnO.
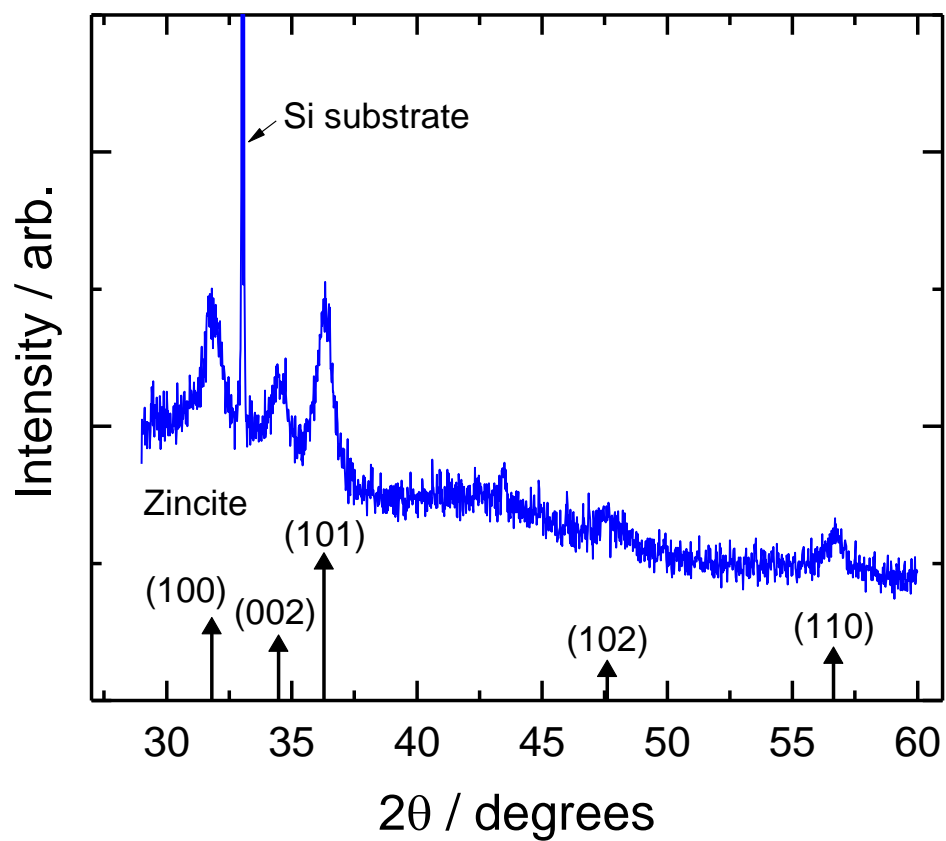
Figure S1. X-ray diffraction pattern of ZnO nanocrystals synthesized at the same conditions as those reported in the paper. These particles were not coated with any atomic layer deposition layers.

Estimation of the percolation threshold.

To estimate the percolation threshold, films were deposited with varied ZnO volume fraction and the resistivity was measured. The nanocrystal size was fixed at 7.3 nm and all films were coated with a sufficient number of Al_2O_3 ALD cycles to fill in the pores. The films were deposited using the previously reported reactor housed in the Chemical Engineering and Material Science Department at the University of Minnesota.[1]   The ZnO volume fraction was varied by changing the pressure ratio across the nozzle, which controls the particle impaction velocity and therefore the resulting film density.[2] Resistivity as a function of the ZnO volume fraction is plotted in Figure S2. The data was fit using the well-known power law expression for the resistivity of a percolated network as a function of conducting phase volume fraction:[3]

$$\frac{\rho}{\rho_0} = \left[\phi(ZnO) - \phi_0\right]^x \tag{S1}$$

where ρ_0 is a constant, $\phi(ZnO)$ is the ZnO volume fraction, x is the scaling exponent and ϕ_0 is the percolation threshold. Ideally x is equal to -2, however, a variety of phenomena can produce deviations from ideality.[4] From the fit of equation (S1) to our data we obtain a percolation threshold of approximately 5% and a scaling exponent of -3.6. In the fit there is some dependency between the parameters ϕ_0 and x, but fits using various initial conditions gave values for the percolation threshold between 5% and 7%. We take the lower value of ϕ_0=5% to perform calculations in the main text.
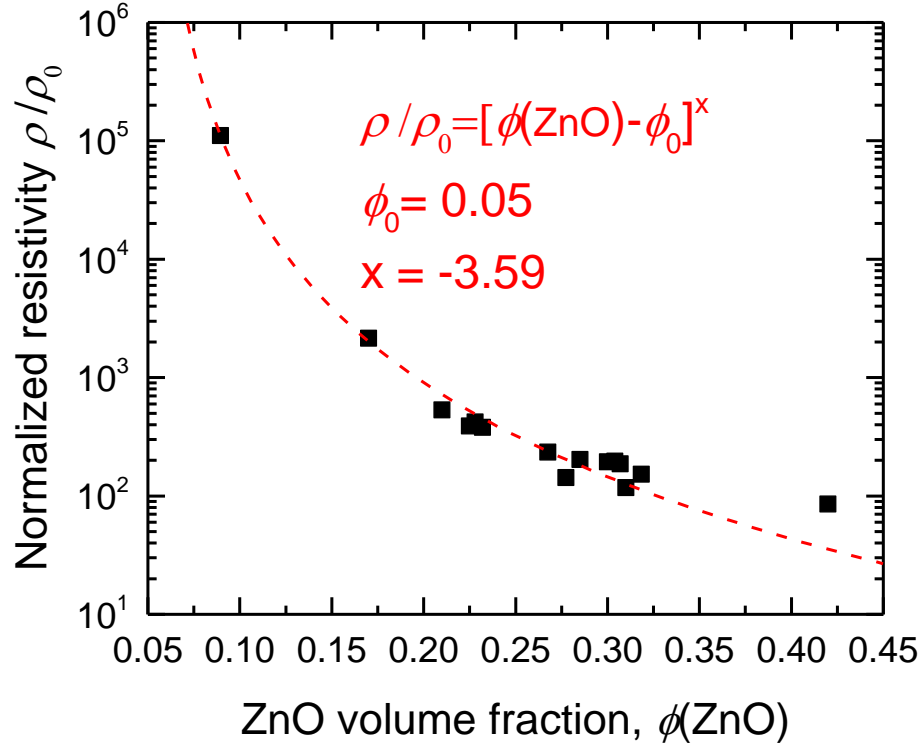
$$\rho/\rho_0 = [\phi(ZnO) - \phi_0]^x$$

$$\phi_0 = 0.05$$

$$x = -3.59$$

Figure S2. Normalized resistivity as a function of ZnO volume fraction for thin films comprised of ZnO nanocrystals embedded in Al_2O_3. The dashed line is the fit of equation (S1) to the data points.

Single particle resistance.

The resistance of a single particle is:[5]

$$R_0 = \frac{\delta}{2e^2 E_{Th}}, \tag{S2}$$

Where δ is the energy level spacing and E_{Th} is the Thouless energy. For spherical particles, the energy level spacing is given by:

$$\delta = \frac{3}{4\pi r_0^3 \nu}, \tag{S3}$$

where ν is the density of states at the Fermi level and r_0 is the particle radius. Since the local

carrier concentration (9×10^{19} cm^{-3}) is well above the Mott transition (7.3×10^{18} cm^{-3}), the grains are

electronically metallic and the free carriers can be modeled as a free electron Fermi gas. The density of

states at the Fermi level for such an electron gas can be calculated as:[6]

$$\nu = \frac{3}{2}\frac{n}{E_f}, \tag{S4}$$

where n is the carrier concentration and E_f is the Fermi energy. The Fermi energy can be calculated as:

$$E_f = \frac{\hbar^2}{2m_e}\left(3\pi^2\,n\right)^{2/3}, \tag{S5}$$

where $\hbar$ is the reduced Planck constant, and m_e is the mass of an electron. Equation (S5) can be

substituted into equation (S4):

$$\nu = \frac{3^{1/3}m_e}{\pi^{4/3}\hbar^2}n^{1/3}, \tag{S6}$$

which can be used to calculate the density of states at the Fermi level if the carrier concentration is

known. The Thouless energy is:[5]

$$E_{Th} = \frac{D_0}{r_0^2} = \frac{k_B T \mu_{local}}{r_0^2 e}, \tag{S7}$$

Where k_B is the Boltzmann constant, T is the temperature, μ_{local} is the local mobility and e is the

elementary charge. Equations (S7), (S6), (S3) and (S2) can be combined to show:

$$R_0 = \frac{\delta}{2e^2 E_{Th}} = \frac{\hbar^2 \pi^{1/3} 3^{2/3}}{8e\,m_e k_B}\cdot\frac{1}{r_0 n^{1/3} T \mu_{local}}\;. \tag{S8}$$

References for Appendix B.

1.   Thimsen, E.; Johnson, M.; Zhang, X.; Wagner, A. J.; Mkhoyan, K. A.; Kortshagen, U. R.; Aydil, E. S. High Electron Mobility in Thin Films Formed *via* Supersonic Impact Deposition of Nanocrystals Synthesized in Nonthermal Plasmas. *Nat Commun* 2014, 5, 5822.

2.   Holman, Z. C.; Kortshagen, U. R. A Flexible Method for Depositing Dense Nanocrystal Thin Films: Impaction of Germanium Nanocrystals. *Nanotechnology* 2010, 21, 335302.

3.   Stauffer, D.; Aharony, A. *Introduction to Percolation Theory*. 2nd ed.; Taylor & Francis: London ; Washington, DC, 1992; p x, 181 p.

4.   Grimaldi, C.; Balberg, I. Tunneling and Nonuniversality in Continuum Percolation Systems. *Phys. Rev. Lett.* 2006, 96.

5.   Beloborodov, I. S.; Lopatin, A. V.; Vinokur, V. M.; Efetov, K. B. Granular Electronic Systems. *Reviews of Modern Physics* 2007, 79, 469-518.

6.   Kittel, C. *Introduction to solid state physics*. 8th ed.; Wiley: Hoboken, NJ, 2005; p xix, 680 p.